Surface symmetry breaking and disorder effects on superconductivity in perovskite $BaBi_3$ epitaxial films

Wen-Lin Wang,[1] Yi-Min Zhang,[1] Nan-Nan Luo,[1] Jia-Qi Fan,[1] Chong Liu,[1] Zi-Yuan Dou,[1] Lili Wang,[1,2] Wei Li,[1,2] Ke He,[1,2] Can-Li Song,[1,2,*] Yong Xu,[1,2,3,†] Wenhui Duan,[1,2,4] Xu-Cun Ma,[1,2] and Qi-Kun Xue[1,2,‡]

[1]*State Key Laboratory of Low-Dimensional Quantum Physics, Department of Physics, Tsinghua University, Beijing 100084, China*

[2]*Collaborative Innovation Center of Quantum Matter, Beijing 100084, China*

[3]*RIKEN Center for Emergent Matter Science (CEMS), Wako, Saitama 351-0198, Japan*

[4]*Institute for Advanced Study, Tsinghua University, Beijing 100084, China*

(Received 20 March 2018; published 22 August 2018)

The structural or electronic symmetry breaking of the host lattice is a recurrent phenomenon in many quantum materials, including superconductors. Yet, how these broken-symmetry states affect the electronic pair wave function of superconductivity has been rarely elucidated. Here, using low-temperature scanning-tunneling microscopy and first-principles calculations, we identify the broken rotational symmetry via stripe ordering on the (001) surface of perovskite $BaBi_3$ films grown by molecular-beam epitaxy, and show that it consequently leads to anisotropic superconductivity with twofold symmetry. In contrast, the structural disorder smears out the anisotropy of electron pairing and fills superconducting subgap density of states as the film thickness is reduced. A quasi-long-range model of superconducting fluctuations is revealed to describe the tunneling conductance spectra of thin $BaBi_3$ films well, and to exemplify how disorders contribute to the low-energy quasiparticle excitations in superconductors. Our findings help understand the effects of symmetry-breaking states and disorders on superconductivity, particularly the existing tunneling conductance spectra there.

DOI: 10.1103/PhysRevB.98.064511

I. INTRODUCTION

Superconductivity often emerges in proximity to and even coexists with a plethora of broken-symmetry states, e.g., charge/spin-density waves [1–5], structural distortion [6,7], electronic nematicity [8–14], static and fluctuating stripes [15–18], etc. These modulated states are inextricably intertwined with superconductivity and lead to very sophisticated phase diagrams, irrespective of whether the nature of superconductivity is conventional or not [19,20]. Recent experimental and theoretical advances have been establishing C_2-symmetric stripe phases as universal in these materials [18,21–25], which are deemed crucial for the formation of Cooper pairs. However, the subtle interrelation between the intriguing phases and superconductivity—-whether they compete [19,21,26], correlate with [8,9,18,22–25], or how they act on the emergent superconducting pairing [27–30]—-remains a hotly debated topic. On the other hand, the occurrence of superconductivity relies mostly on chemical dopants or interface engineering, which turn out to be potential sources of disorder to intertwine with the existing broken-symmetry states and superconductivity [31–35], masking many intrinsic effects. For superconductors with such a variety of interactions, tracing the respective roles of symmetry breaking and disorder played in superconductivity remains essential but challenging in experiment. It necessitates the exploration of simple superconducting systems where the symmetry-breaking and disorder effects can be easily controlled.

In the present study, we introduce a nonoxide perovskite superconductor $BaBi_3$ with tetragonal crystal structure of space group $P4/mmm$ as shown in Fig. 1(a). Its bulk becomes superconducting below a critical temperature $T_c = 5.9$ K [36], recently being studied for pursuing novel electronic states related to the strong spin-orbit coupling of Bi [36–38]. Remarkably, $BaBi_3$ has a much simpler structure as compared with other perovskite oxide superconductors (e.g., cuprates [3,5,7–9,16,21,22,26] and bismuthates [18]), and offers an ideal platform to experimentally elucidate the effects of symmetry breaking and disorder on the electronic pair wave function of superconductivity. We grow $BaBi_3$ epitaxial films with fine control of film thickness on $SrTiO_3(001)$ substrates using state-of-the-art molecular-beam epitaxy (MBE) technique. Our scanning-tunneling microscopy (STM) study reveals a series of stripelike structures on the surface of $BaBi_3$ epitaxial films, which breaks the C_4 rotational symmetry of the host crystal, and also structural disorder induced by the $SrTiO_3(001)$ substrates, which enhances in strength with reducing film thickness. Tunneling experiments discover twofold anisotropic superconducting gap function by surface symmetry breaking in the thick films, but reveal in the thin films that disorder smears out the gap anisotropy, fills the subgap density of states (DOS), and suppresses superconducting coherence peaks. We find that the resultant "soft" spectral gaps in disordered thin films are all satisfactorily modeled in the framework of quasi-long-range superconducting fluctuations.

II. METHODS

All the experiments were performed in an ultrahigh vacuum cryogenic STM apparatus equipped with a MBE system for

*clsong07@mail.tsinghua.edu.cn
†yongxu@mail.tsinghua.edu.cn
‡qkxue@mail.tsinghua.edu.cn

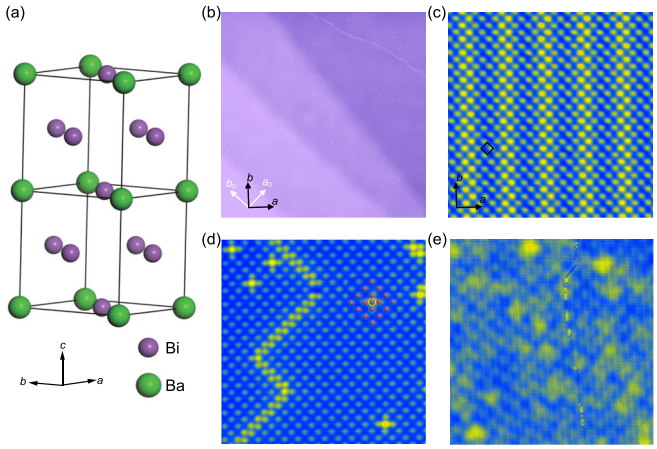

FIG. 1. Morphology and surface structure of $BaBi_3$ films. (a) Schematic crystal structure of nonoxide perovskite superconductor $BaBi_3$. The a, b, and c axes are aligned along the crystallographic orientations. (b) STM topography ($V = 1.5$ V, $I = 30$ pA, 300 nm × 300 nm) of ~22-UC-thick $BaBi_3$ epitaxial films on $SrTiO_3(001)$. The principal directions of $SrTiO_3(001)$ surface run along the a_0 and b_0 axes. (c) A zoom-in view of $BaBi_3(001)$ surface ($V = 5$ mV, $I = 100$ pA, 16 nm × 16 nm) exhibiting stripelike order. The black square indicates the unit cell of $\sqrt{2} \times \sqrt{2}$ reconstructed surface. Every bright spot denote the top Bi atoms. (d) Atomic resolution STM image of $BaBi_3$ films grown under Bi-richer atmosphere ($V = -30$ mV, $I = 130$ pA, 16 nm × 16 nm), presenting Bi-site adatoms (see the overlaid Bi balls). The surface strips are visually overcome by addition of high-contrast defects. (e) STM image on 5-UC films ($V = 10$ mV, $I = 200$ pA, 100 nm × 100 nm), exhibiting the coexistence of surface stripe and moiré superstructure.

in situ sample preparation (Unisoku). The base pressure for both systems is better than $<1.0 \times 10^{-10}$ Torr. Nb-doped $SrTiO_3(001)$ substrates (0.05 wt. %) were degassed at 600 °C for 3 h, and then annealed at 1250 °C for 20 min to obtain clean surface. The samples studied, namely $Ba(Sr)Bi_3$ crystalline films, were epitaxially grown on $SrTiO_3$ substrate by coevaporating high-purity Ba(Sr) (99.9%) and Bi (99.997%) sources from their respective Knudsen cells, with the substrate held at 340 °C (240 °C). The growth rate was approximately 0.1 unit cell per minute. By varying the growth duration, the film thickness can be controlled as wanted. After MBE growth, the samples were *in situ* transferred from MBE chamber to STM stage for topographic and spectroscopic measurements. Prior to data collection, polycrystalline PtIr tip was cleaned by electron-beam bombardment and appropriately calibrated on Ag/Si(111) films. Tunneling conductance dI/dV spectra and zero-bias conductance (ZBC) maps were acquired at 0.4 K by disrupting the feedback circuit, sweeping the sample voltage V, and recording the differential conductance dI/dV value using a standard lock-in technique with a small bias modulation of 0.1 mV at 913 Hz, unless other specified. The tunneling gap for all dI/dV spectra and maps is set at $V = 10$ mV and $I = 200$ pA, unless otherwise specified.

First-principles calculations were performed within the framework of density-functional theory (DFT), as implemented in the Vienna *Ab initio* Simulation Package [39]. The Perdew-Burke-Ernzerhof exchange correlation [40], the projector-augmented-wave potential [41], and the plane-wave basis with an energy cutoff of 400 eV were employed. The period slab approach was applied to model the $BaBi_3$ and $SrBi_3$ surfaces, which utilized a six-layer slab with the bottom two layers fixed during structural relaxation and a vacuum layer of ~13 Å. Structural optimization was performed using a force convergence criterion of 0.01 eV/Å. 12×12×12, 10×10×1, and 5 × 5 × 1 Monkhorst-Pack k grids together with a Gaussian smearing of 0.05 eV were used in self-consistent calculations of bulk, $\sqrt{2} \times \sqrt{2}$, and $2\sqrt{2} \times 2\sqrt{2}$ surface supercells, respectively. The spin-orbit coupling was included in all the calculations except for structural relaxation. STM images were simulated by the local DOS based on the Tersoff-Hamann approach [42]. The surface formation energy was calculated as a function of atomic chemical potential μ_i for a $\sqrt{2} \times \sqrt{2}$ surface supercell that has n_i atoms of the i_{th} species more than the reference surface (i.e., the ideal Ba-Bi or Sr-Bi terminated surface): $\Delta E = E - E_0 - \sum_i n_i \mu_i$, where E and E_0 are the total energies of the given and reference surfaces, respectively. The calculated bulk lattice constants are $a = b = 5.174$ Å and $c = 5.130$ Å for $BaBi_3$ and $a = b = c = 5.081$ Å for $SrBi_3$.

III. RESULTS AND DISCUSSION

A. MBE growth and surface structure characterization

Figure 1(b) depicts a constant-current STM topographic image of as-prepared $BaBi_3$ films, which straddle continuously over the underlying $SrTiO_3$ step edges. This bears a similarity with that of MBE-grown $\beta-Bi_2Pd$ films [43]. Shown in Fig. 1(c) is a magnified STM image of $BaBi_3$ with a square lattice structure, presenting a preferential growth of epitaxial films along the (001) direction. This is unambiguously confirmed by analysis of the moiré superstructure of $BaBi_3$ films on $SrTiO_3$ (Figs. S1 and S2), as explained in Supplemental Material [44]. The spacing of neighboring bright spots is measured to be approximately 7.4 Å, which is about $\sqrt{2}$ times of the lattice constant $a = 5.188$ Å of $BaBi_3$ in the a-b plane [37]. This means a $\sqrt{2} \times \sqrt{2}$ reconstructed structure formed on the surface. Notably point defects are observed to occupy the hollow sites of the square spots [Fig. 1(d)], as a higher flux ratio of Bi/Ba is used during the film growth.

In addition to the $\sqrt{2} \times \sqrt{2}$ surface reconstruction, another prominent feature of the surface is the occurrence of various stripelike patterns [Figs. 1(c) and S3], which run along either the [1 0 0] or [0 1 0] azimuths (a or b). These stripe patterns are differently spaced and have a dominant separation of $6a$ (Fig. S3), resembling a devil's staircase behavior. The stripe height is measured to be 0.1 Å at 5 mV. It should be emphasized that both the $\sqrt{2} \times \sqrt{2}$ reconstruction and stripes (which always run along either the a or b axes) are universally recognized on $BaBi_3$ regardless of the film thickness, although the fourfold periodic ripples from moiré patterns triumph over the stripe corrugation and render them not easily visible in ultrathin films [Fig. 1(e)]. Here the moiré superstructure-induced ripples distort the crystal lattice and serve as potential scatters to influence the superconducting pairing of $BaBi_3$ [29–32]. Thus far, the stripe phases, breaking the C_4 rotational symmetry, in conjunction with the tunable structural disorder from the moiré ripples by varying the

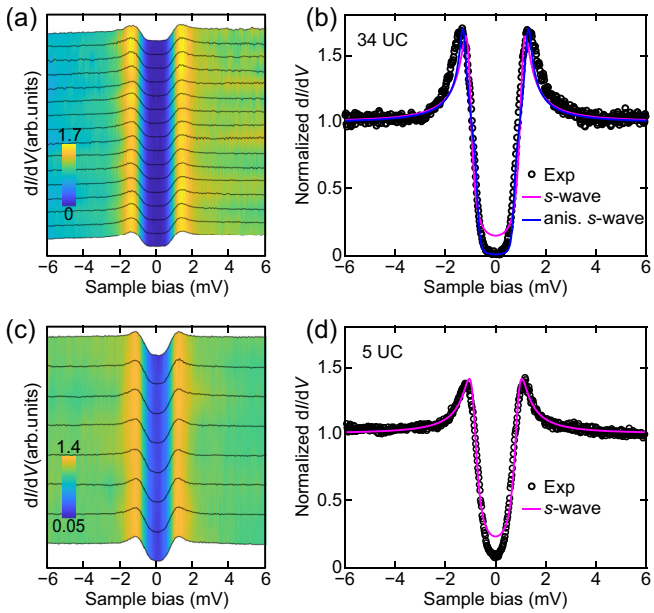

FIG. 2. Tunneling spectroscopy. (a) Spatially resolved differential conductance dI/dV spectra at 0.4 K, taken on a 272 nm × 272 nm (4 × 4 grid) region of ∼34-UC $BaBi_3$ films, illustrating the spatial homogeneity. (b) Normalization of the averaged dI/dV spectra (empty circles) and its best fits to the Dynes formula with s-wave (magenta line)- and anisotropic s-wave (blue line)-gap functions, respectively. The experimental data show a better fit to the twofold symmetric gap function $\Delta = 1.01 + 0.28\cos(2\theta)$ meV. (c) Equally spaced dI/dV spectra, and (d) normalized dI/dV spectrum as well as its best fit to a single s-wave gap on 5-UC films.

film thickness, make $BaBi_3$ a promising research platform for exploring the interplay between symmetry breaking, disorder, and superconductivity.

B. Gap spectroscopy and vortex structure in the superconducting state

In order to find the effect of symmetry breaking on superconductivity, we firstly measured the differential conductance dI/dV spectra on 34-unit-cell (UC)-thick $BaBi_3$ epitaxial film with small moiré ripple. Here the film thickness is determined by measuring its height from the substrate and dividing it by the out-of-plane lattice constant of 5.130 Å, owing to the island growth mode of $BaBi_3$ on $SrTiO_3$ [Fig. S1(a)]. The tunneling spectra are typified in Fig. S4, where a superconducting gap near the Fermi level (E_F) is clearly visible. Plotted in Fig. 2(a) are a series of superconducting gaps acquired on a region of 272 nm × 272 nm at 0.4 K. The tunneling gaps all exhibit vanishing spectral weight over a finite energy range near E_F and two clear coherence peaks at the gap edges. These features, characteristics of full-gap superconductivity [35], provide tunneling evidence of no gap node in the superconducting pairing function of $BaBi_3$, as anticipated. To compare the experimental curves with theoretical ones, we normalize the tunneling conductance by dividing the spatially averaged dI/dV spectrum by its background (that is extracted from a linear fit to the conductance for $|V| > 3.5$ mV) and illustrate it in Fig. 2(b) as black symbols. In theory, such spectrum can be described by the BCS Dynes formula with an effective energy broadening Γ [45],

$$\frac{dI}{dV}(V) \cong \mathrm{Re}\left[\frac{V - i\Gamma}{\sqrt{(V - i\Gamma)^2 - \Delta^2}}\right]. \quad (1)$$

Attempts to fit the experimental data in Fig. 2(b) with a BCS s-wave isotropic gap Δ based on Eq. (1) are never successful. The best fitting (magenta line), which does not yet explain well the local DOS near E_F, yields a gap magnitude Δ of 1.06 meV and unreasonably large Γ of 0.15 meV. Although a smaller Γ will remove the spectral weight near E_F and lead to the experimentally observed flat bottom, it gives rise to very sharp coherence peaks, making the global fitting even worse.

The situation is exacerbated as the tunneling spectra of thinner $BaBi_3$ films are concerned. Figure 2(c) represents eight dI/dV spectra along a 73-nm trajectory on 5-UC-thick film. As compared to those on thick films [Figs. 2(a) and 2(b)], the coherence peaks are more appreciably suppressed and the subgap DOS near E_F is significantly lifted. The resultant V-shaped soft gaps lie as well beyond the conventional BCS s-wave prediction, as exemplified in Fig. 2(d).

Vortex imaging of type-II superconductors provides unique capability to bring insight into superconducting gap structure. Figures 3(a)–3(c) display spatial-resolved ZBC maps on $BaBi_3$ epitaxial films of varying thickness, with the magnetic fields applied perpendicular to the ab plane of $BaBi_3$. The superconducting order parameter vanishes within the vortex cores, allowing ZBC maps to reveal vortex cores as yellow regions with enhanced ZBC. Intriguingly, their shapes are dependent on the thickness of $BaBi_3$ films, and exhibit a gradual crossover from elliptical [Fig. 3(a)] to circular [Fig. 2(c)] as the film thickness decreases. A close scrutiny of the elliptical vortices and the corresponding STM topographies reveals that they are always elongated along the surface stripes [cf. Fig. 3(d) and Fig. 3(e) or Fig. 3(b) and Fig. S5]. It is worth noticing that two orthogonal stripes could intersect to form grain boundaries [Figs. S3(f) and S3(g)], across which the long and short axes of elongated vortex cores interchange [Fig. 3(b)]. These observations compellingly establish a close link between the vortex core structure and surface stripes.

Previously, the elongated vortices have been observed only rarely in cuprate superconductor $YBa_2Cu_3O_{7-\delta}$ with ab-plane anisotropy ($a \neq b$) [46], FeSe with strong electronic nematicity [28], and quasi-one-dimensional compound $Ta_4Pd_3Te_{16}$ [47,48] and Ni-Bi compounds [49]. In principle, the elongated vortex cores can be readily accounted for by the anisotropy of superconducting coherence length ξ, which scales with Fermi velocity v_F and $1/\Delta$ via $\xi = \hbar v_F/\pi\Delta$. knowing that the surface-stripe phases work as the only source for breaking the fourfold symmetry of $BaBi_3$, we claim that it is the surface-stripe phase to generate the twofold anisotropy in v_F and/or Δ, and consequently lead to the elongated vortices on thick films. On the other hand, the circular vortex cores on thin $BaBi_3$ films, despite the preservation of surface stripe, imply that other factors are involved to kill the anisotropy in v_F and/or Δ. Since we prepared the $BaBi_3$ films using the same recipe, the observed differences between thick and thin films are probably caused by a strength distinction of moiré ripples. A straightforward explanation would be that

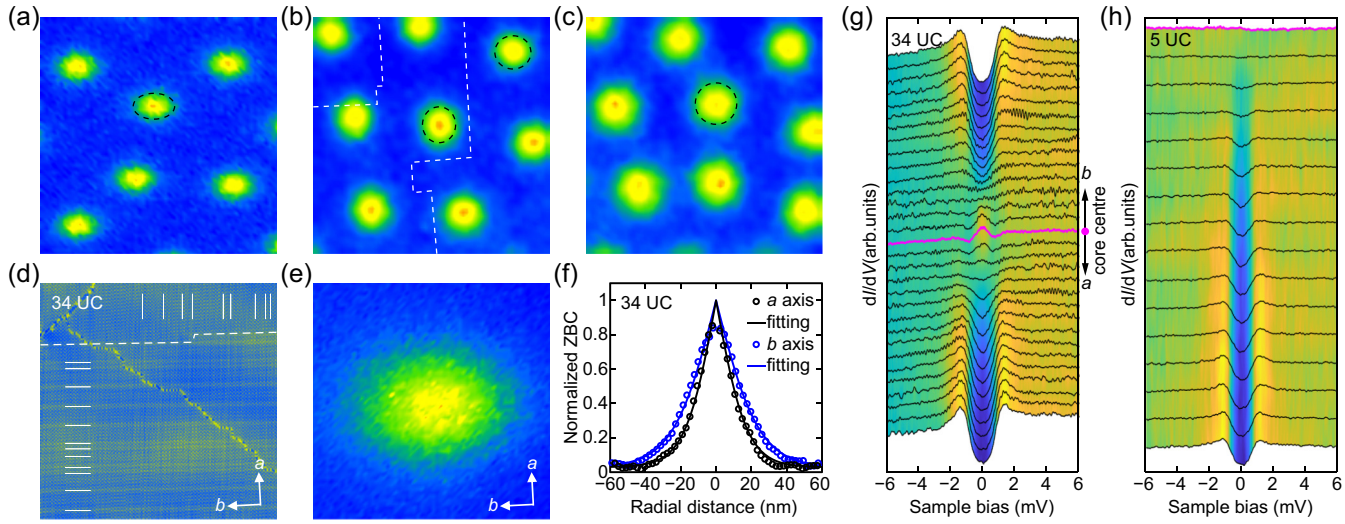

FIG. 3. Vortex core structure and bound states. (a)–(c) Thickness-dependent internal structure of vortex cores on $BaBi_3$ films, with the thickness d of (a) 34, (b) 11, and (c) 5 UC. The applied magnetic field and STM image sizes are (a), (b) 0.2 T, 272 nm × 272 nm and (c) 0.5 T, 182 nm × 182 nm, respectively. Dashed ellipses or circles draw the periphery of vortex cores, showing a transition from elliptical to circular vortex core with reduced film thickness. The white dashed lines designate grain boundaries, separating regions with orthogonal orientations of surface stripes and vortices. (d) High-resolution STM topography ($V = 10$ mV, $I = 200$ pA, 73 nm × 73 nm) on 34-UC films, and (e) simultaneous ZBC map showing a single vortex at 0.05 T, revealing the vortex elongation along the surface stripes. The thin white lines mark the surface stripes for easy viewing. (f) Radial dependence of ZBC in (e), and the fits to the Ginzburg-Landau theory. (g) Tunneling dI/dV spectra measured at equally spaced (2.8-nm) distance across the vortex core of (e), exhibiting clear bound states at the vortex center of 34-UC films (magenta curve). (h) dI/dV spectra across a vortex core of 5-UC films, presenting no ZBC peak. Setpoint: $V = 10$ mV, $I = 100$ pA.

the moiré ripples cause strong electron scattering and smear out the gap anisotropy of Δ in thin films, considering that disorder scattering typically has minor influence on the band structure and the corresponding v_F. In other words, it is the surface-stripe phase that breaks the C_4 symmetry and leads to a twofold symmetric superconducting gap Δ and elongated vortices on thick films, while the structural disorders from moiré ripples tend to kill the gap anisotropy and result in the circular-shaped vortex cores on thin films. Indeed, by using a twofold symmetric gap function $\Delta(\theta) = \Delta_1 + \Delta_2 \cos(2\theta)$, the theoretical curve [blue line in Fig. 2(b)] well reproduces the results of thick $BaBi_3$ films, yielding $\Delta_1 = 1.01$ meV and $\Delta_2 = 0.28$ meV. The quantitative agreements, both at the gap bottom and near the coherence peaks, confirm the twofold symmetric gap function on thick $BaBi_3$ films.

To quantify the elongation of vortex cores on 34-UC-thick film (the thickest one we studied), the radial dependences of vortex-induced ZBC variations acquired along and perpendicular to the stripes are plotted in Fig. 3(f). Based on the Ginzburg-Landau description of the order parameter near a superconductor-metal interface [47,48], the ZBC profile across the vortex core obeys $Z(r) = Z_\infty + (1 - Z_\infty)[1 - \tanh(-r/\sqrt{2}\xi)]$, where $Z(r)$ represents the normalized ZBC at the distance r to the vortex core. The best fits to our experimental data yield the superconducting coherence length $\xi_a = 12.4$ nm, $\xi_b = 17.3$ nm, and the anisotropy $\xi_b/\xi_a = 1.4$. The averaged coherence length $\bar{\xi} = \sqrt{\xi_a \xi_b} = 14.6$ nm is close to the reported values of bulk $BaBi_3$ superconductor [36,38]. This value appears several times larger than the separations between adjacent stripe patterns [Figs. 1(c) and S3]. It is therefore anticipated that the surface stripes would lead to an anisotropic pair potential and order parameter Δ [Fig. 2(b)], but little alter the *dI/dV* spectra in the microscopic scale [47,48]. Otherwise, the superconducting correlation function, electronic DOS, and the superconductivity will be localized like nanoscale stripe structure, and spatially inhomogeneous superconducting gaps might be observed across the stripes.

The twofold symmetric pairing in thick $BaBi_3$ films is further evidenced by studying the spatial evolution of dI/dV spectra in the vicinity of a single vortex, as shown in Fig. 3(g). At the very center of vortex core, a prominent ZBC peak, which we attribute to the Andreev bound states originating from the constructive interference between electronlike and holelike quasiparticles within vortices [50], is clearly identified. The ZBC peaks decay outside the vortex core, but behave differently along the a and b axes. Although the bound states along the a axis completely vanish, they stay discernible along the b axis, at a distance $r = 8.4$ nm from the vortex center. No splitting of the ZBC peak is resolvable when measured away from the vortex center [Fig. 3(g)]. This is possibly caused by the small energy level spacing $\varepsilon_0 = \Delta^2/E_F$ of the discrete vortex bound states [44], which is exceeded by the thermal broadening of 0.4 K, but also probably by the disorder-induced intrinsic broadening of the quasiparticle states. The latter is actually implied by exploring the vortex core excitations of thin films. As displayed in Fig. 3(h), no ZBC peak can be observed at the vortex center of 5-UC films, where the enhanced disorder scattering significantly reduces the electron mean-free path ℓ and pushes the thin films to the dirty limit ($\ell < \xi$, no constructive interference of quasiparticles and thus no ZBC peak). Here the transition of $BaBi_3$ films from the clean ($\ell > \xi$) to dirty limit bears a strong resemblance to the previously observed ones in $2H$-$Nb_{1-x}Ta_xSe_2$ and Pb [51,52],

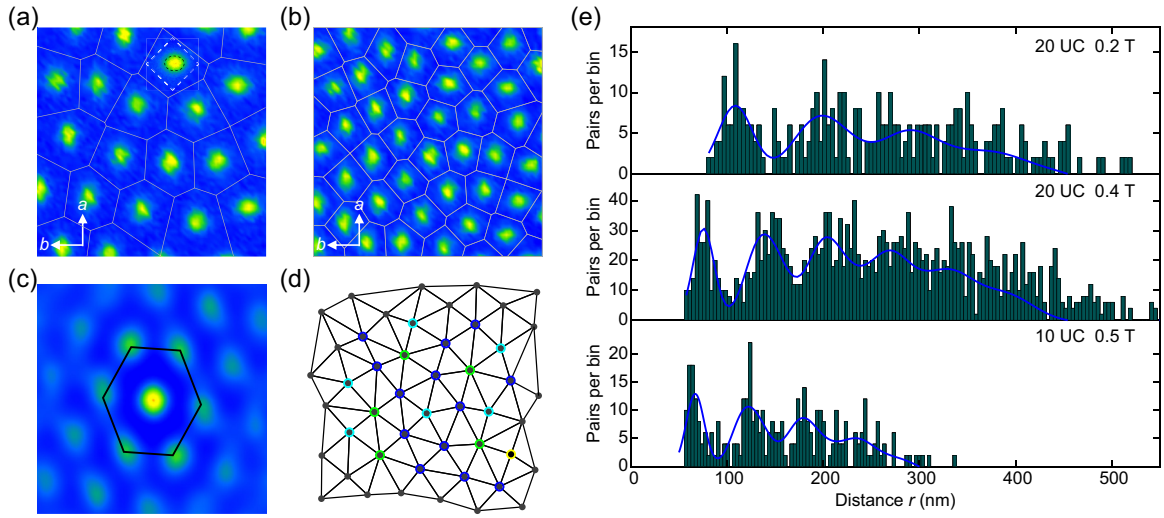

FIG. 4. Vortex configuration. (a), (b) Magnetic vortex lattices (454 nm × 454 nm) of ~20-UC-thick $BaBi_3$ films at 0.2 and 0.4 T, respectively. Voronoi cells (white lines) are overlaid onto the vortex maps. The white dashes mark one high-resolution vortex core that is also elongated along the surface stripes. (c) Two-dimensional autocorrelation function calculated from vortex map in (a), indicative of distorted hexagonal lattice (black polygon). (d) Delaunay triangulation diagram (gray lines) of the vortex map in (b). Every vortex has been color-coded based on its coordination number (yellow, 4; cyan, 5; blue, 6; green, 7). (e) Histograms of vortex pair distances d_{ij} at varying film thickness and field. Blue lines show the best fits of the experimental RDF to Eq. (3).

triggered by the chemical [51] and interfacial disorder [32], respectively.

Notably, the twofold symmetric gap observed on thick $BaBi_3$ films [Fig. 2(b)] does not mean that the bulk $BaBi_3$ is characteristic of anisotropic order parameter Δ. Instead, the bulk superconducting gap Δ should be isotropic [34], since the stripes occur primarily at the top surface and no symmetry breaking is involved in bulk. Considering the STM sensitivity to surface DOS, the measured *dI/dV* spectra have their origin from the anisotropic surface order parameter Δ caused by the stripe phases there, leaving the bulk DOS inaccessible. As the magnetic vortices penetrate through the surface-near regions, the internal cores are subject to the anisotropic pair potential and will be elliptically deformed for energetically favorable state, just as those of anisotropic superconductors [47,48].

The disorder response of vortex configuration has also been studied by mapping the spatial ZBC on a larger field of view of 454 nm × 454 nm, with the same pixels of 64 × 64. To better visualize the vortices, we find every vortex center by the local ZBC maximum and draw the Voronoi cells on the ZBC maps in Figs. 4(a) and 4(b). From the calculated Voronoi cell size, we estimate the average flux per vortex $\Phi_0 = 2.05 \times 10^{-15}$ Wb, consistent with a single flux quantum of 2.07×10^{-15} Wb. Evidently, vortices do not arrange into the ordered hexagonal or square lattice. Instead, a distorted hexagonal lattice is justified from the autocorrelation image of vortex lattice, as illustrated in Fig. 4(c). This underscores the role of vortex pinning played primarily by the structural disorders of epitaxial $BaBi_3$ films. Figure 4(d) shows the Delaunay triangulation analysis of Fig. 4(b), in which every vertex denotes the position of vortex and is color-coded by its coordination number. Only half of vortices are sixfold coordinated, affirming the occurrence of vortex pinning in $BaBi_3$ films.

We further evaluate the vortex pinning by measuring the relative distances $d_{ij} = |r_i - r_j|$ for all vortex pairs at positions r_i and r_j. The histograms of such distances are plotted in Fig. 4(e), which should approximate the radial distribution function (RDF) of vortex lattice [53,54],

$$f(r) = \sum_{n=1}^{\infty} \frac{N_n}{\sigma\sqrt{2\pi R_n/a_\Delta}} \exp\left[-\frac{(r-R_n)^2}{2\sigma^2 R_n/a_\Delta}\right], \quad (2)$$

where $a_\Delta = \sqrt{2\Phi_0/\sqrt{3}H}$ is the expected lattice constant for a perfect hexagonal vortex lattice at the magnetic field of H, $\sigma \ll a_\Delta$ is the standard deviation of the discrepancy between nearest-neighbor distances, R_n is the radius of the nth coordination shell, and N_n is the number of sites in this shell. The oscillatory blue curves show the fits of the experimental histograms to

$$Nf(r)\delta r \frac{\pi L^2 + (4-r)r^2 - 4rL}{\pi L^2}, \quad (3)$$

with N and δr representing the involved vortex number and bin size of the histograms, respectively. The fractional term accounts for the finite image size. Here only two free parameters R_1 and σ are relevant. Their values as well as the correlation length ζ of vortex lattices, estimated from a_Δ and σ [53], are summarized in Table S2 [44]. The values of ζ are two or three times as large as a_Δ for varying film thickness and H, indicative of mediate pinning forces by the structural disorders in $BaBi_3$ films. It is worth noting that the fitted parameter R_1 deviates from a_Δ ($R_1 < a_\Delta$) with reduced film thickness and increasing H [the bottom and middle panels in Fig. 4(e)]. It might be because the fourfold moiré ripples tend to configure vortices into square lattices, but are not strong enough to result in regular ones. This is evident by analysis of the autocorrelation images (Fig. S6). Distinct from Fig. 4(c), the central rings are nearly square-shaped with the sides running along the directions of moiré ripples.

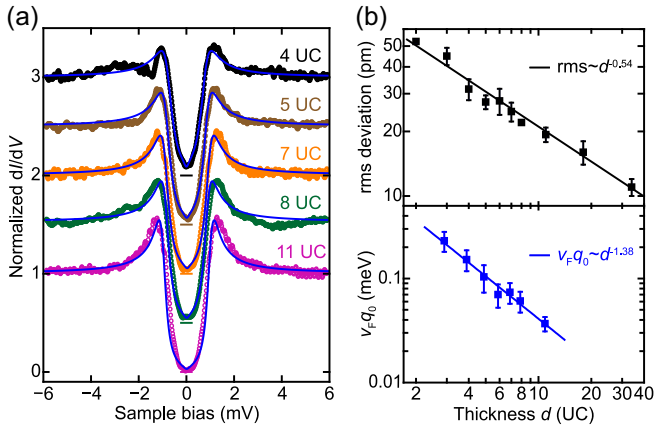

FIG. 5. Correlation between superconducting gap and disorder. (a) Film thickness dependence of $\mathrm{d}I/\mathrm{d}V$ spectra on $BaBi_3$ thin films. Blue lines show the best fits to the model of quasi-long-range superconducting fluctuations in Eq. (4). The spectra have been vertically offset for clarity, with the zero conductance positions marked by the correspondingly colored horizontal lines. (b) Double-logarithmic plots of fluctuation strength $v_F q_0$ (bottom panel) and rms deviation (top panel) caused by the moiré ripple vs film thickness d. They scale as $d^{-0.38\pm0.08}$ and $d^{-0.54\pm0.03}$ with d. The error bars denote the standard deviation from 60 STM images and fits of 50 $\mathrm{d}I/\mathrm{d}V$ spectra.

C. Correlation between disorder and superconducting gap

In order to assess the impact of disorder on the superconducting gap, the tunneling conductance spectra on thin $BaBi_3$ films with varying thickness are taken and plotted in Fig. 5(a). As the film thickness is reduced, the increased structural disorders gradually suppress the coherence peaks, fill and sharpen the subgap DOS near E_F, and lead eventually to V-shaped soft gap structure. These spectra look analogous to those widely observed in highly disordered superconductors [32,33,55–60], and deviate substantially from Eq. (1) with either isotropic or anisotropic s-wave-gap functions (Fig. S7 and Table S3), as explained in Supplemental Material [44]. Recently, a model of finite-range superconducting fluctuations has been put forward for disordered superconductors [33,61,62]. In this model, instead of the effective energy broadening Γ ($\Gamma = 0$) in Eq. (1), a superconducting correlation length $1/q_0$ is considered to calculate the tunneling spectrum. Interestingly, we find that all the experimental $\mathrm{d}I/\mathrm{d}V$ spectra in thin $BaBi_3$ films can be well described by the quasi-long-range superconducting fluctuation [61], namely

$$\Delta^2(V) = \frac{\Delta_0^2}{\pi^2}\frac{V}{\sqrt{v_F^2 q_0^2 + V^2}}\left[\ln\left(\frac{\sqrt{v_F^2 q_0^2 + V^2} + V}{\sqrt{v_F^2 q_0^2 + V^2} - V}\right) - i\pi\right]. \tag{4}$$

Here a small $v_F q_0$ means a slow spatial decay of pair function $\Delta(r)$. As the pair function Δ does not decay ($q_0 = 0$), one recovers the well-known BCS result. Figure 5(b) summarizes the film-thickness-dependent $v_F q_0$ extracted from the best fits to Eq. (4) [blue curves in Fig. 5(a)], and disorder strength characterized by the rms deviation of STM image corrugation. Evidently, they reduce and scale with the film thickness in a power-law manner, e.g., $v_F q_0 \propto d^{-1.38}$. This establishes a direct linkage between the moiré ripple-induced disorders and the gap softening. The disorders tend to increase the spatial decay of $\Delta(r)$ and suppress the coherence peaks in superconductors.

Notably, although the fluctuating model quantitatively follows the experimental $\mathrm{d}I/\mathrm{d}V$ spectra of $BaBi_3$ films with strong disorders, it lacks the validity by degrees with attenuating disorder on thick films, e.g., 11-UC film in Fig. 5(a), where surface stripes and disorders are intertwined and cooperatively affect the tunneling conductance spectra. The observation of slightly elongated vortex cores on such films supports this claim [Fig. 3(b)]. On the other hand, the moiré ripples, despite being invisible from STM topography [Fig. 1(c)], play yet an essential role in superconductivity of the thickest films we investigated, justified by two observations. First, there remains a tiny discrepancy (e.g., near the gap edges) between the experimental $\mathrm{d}I/\mathrm{d}V$ curve and the theoretical one in Fig. 2(b). From the fitting parameters of $\Delta_1 = 1.01$ meV and $\Delta_2 = 0.28$ meV, we extract a gap anisotropy of 1.77, larger than the anisotropy $\xi_b/\xi_a = 1.4$. This is primarily derived as a consequence of disorder, which kills the coherence peaks and leads to an overestimation of gap anisotropy in the theoretical fit. Second, an oblique vortex lattice is often observed for elongated vortices as the pinning is not effective [28,46–48], due to a trade-off between the direction-dependent vortex-vortex interactions expected for elliptic vortices and the closest packing of vortices. However, imposed by the moiré ripple-induced fourfold vortex pinning perturbation, this trade-off would be disturbed, leading to a nearly random arrangement

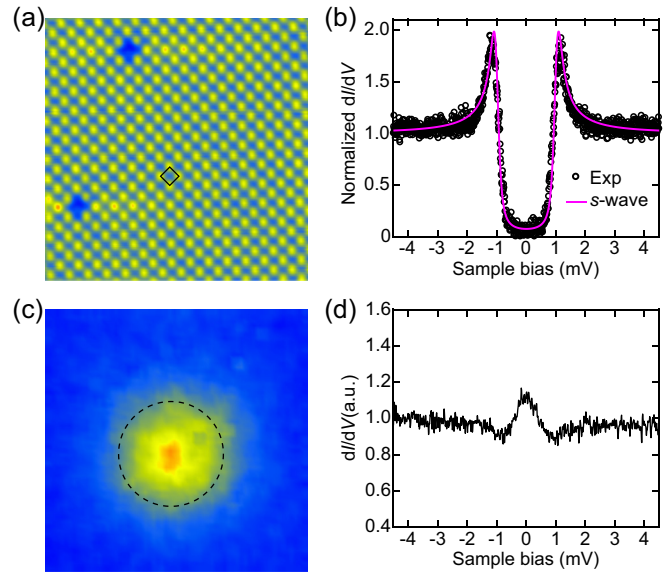

FIG. 6. STM characterization of $SrBi_3$ films. (a) Atomically resolved STM image ($V = 5$ mV, $I = 100$ pA, 16 nm × 16 nm) on ~28-UC $SrBi_3$ epitaxial films, presenting two Bi-site vacancies. The black square marks the $\sqrt{2} \times \sqrt{2}$ surface reconstruction, with a periodicity of about 7.2 Å. (b) Tunneling spectrum ($V = 5$ mV and $I = 100$ pA) of $SrBi_3$ (black circles), and the best fit to the Dynes formula in Eq. (1), with an isotropic s-wave pairing gap (magenta line). (c) ZBC map showing a circular-shaped vortex core (black dashes) on $SrBi_3$. (d) Bound state at the vortex center. Set point: $V = 5$ mV and $I = 100$ pA.

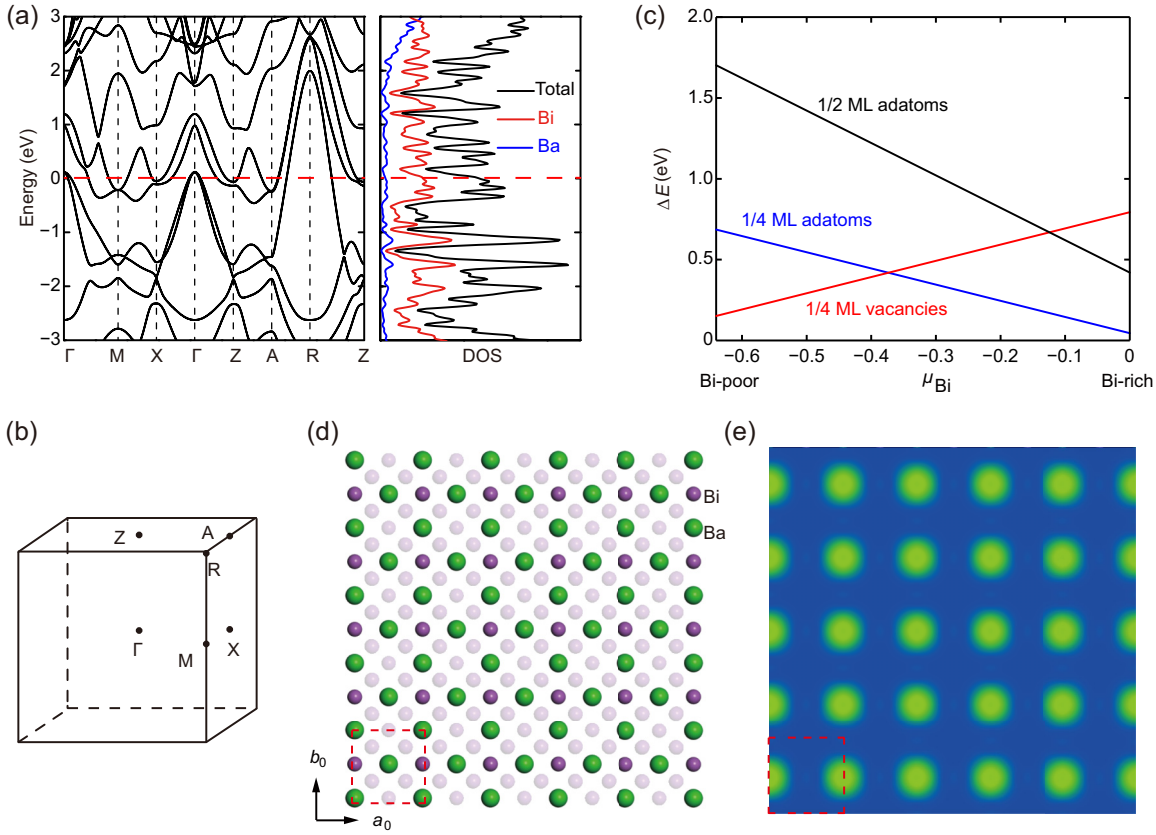

FIG. 7. DFT calculations of $BaBi_3$. (a) Electronic band structure and DOS of bulk $BaBi_3$. (b) The Brillouin zone of bulk $BaBi_3$ and high-symmetry K points. (c) Surface formation energy (ΔE) of $\sqrt{2} \times \sqrt{2}$ reconstructed $BaBi_3(001)$ surfaces as a function of the chemical potential of Bi, referenced to the Ba-Bi terminated surface, with $\mu_{Bi} = 0$ corresponding to bulk Bi. (d) Top-view atomic structure of the Ba-Bi terminated surface with 1/4-ML Bi vacancies, and (e) its simulated STM image taken at 0.1 eV above E_F. A surface supercell is outlined by red dashed lines. Atoms in deep layers are shaded for clarity.

of vortices, as revealed in Fig. 3(a). Further theoretical studies of anisotropic superconductors subject to strong disorder scattering may help fully understand the above tunneling spectra.

D. Superconductivity and vortex core of $SrBi_3$

To gain further understanding regarding the interplay between symmetry breaking and superconductivity, we examine the tunneling dI/dV spectrum at 0.4 K for another superconducting sister compound $SrBi_3$ with an almost identical T_c (~5.6 K) for comparison. The substitution of Ba by Sr changes the crystal from tetragonal to cubic structure (space group $Pm-3m$) with a lattice constant of ~5.055 Å [37,38]. Figure 6(a) depicts an atomically resolved STM image of 28-UC $SrBi_3$ (~14.2 nm) epitaxial films on $SrTiO_3(001)$ substrate, exhibiting again a $\sqrt{2} \times \sqrt{2}$ surface reconstruction marked by the black square. Despite this similarity, one remarkable difference is that unlike $BaBi_3$ no surface stripe is observed in $SrBi_3$. Tunneling spectrum on $SrBi_3$ reveals a fully gapped superconducting DOS that can be nicely fitted to the Dynes formula with an isotropic gap function $\Delta = 1.01$ meV [Fig. 6(b)]. Moreover, a circular-shaped vortex core [Fig. 6(c)] and clear ZBC peak [Fig. 6(d)] at the vortex core are demonstrated on $SrBi_3$ films when a magnetic field of 0.08 T is applied. This is in line with little disorder and negligible gap anisotropy involved in $SrBi_3$ films, which does not suffer from surface symmetry breaking.

E. Atomic and electronic structure calculations of Ba(Sr)Bi_3

We theoretically studied the atomic and electronic structures of $Ba(Sr)Bi_3$ surfaces by density-functional theory. Let us first discuss about $BaBi_3$. The bulk shows a metallic band structure [Figs. 7(a) and 7(b)], as reported previously [37]. While $6p$ orbitals of Ba are mostly located far above E_F (i.e., unoccupied), $6p$ orbitals of Bi are partially occupied and have a dominant contribution to states near E_F [Fig. 7(a)]. Therefore transport-related properties are majorly determined by Bi, suggesting that the bright spots in STM topographies [Figs. 1(c) and 1(d)] can be assigned to Bi atoms.

The $BaBi_3$ bulk is composed of alternating layers of mixed Bi-Ba and pure Bi planes stacked along the (001) direction, giving two types of bulk-terminated (001) surfaces. Given that Ba ($0.34\,J/m^2$) has a smaller surface energy than Bi ($0.43\,J/m^2$) [63] and tends to enrich the surface, the observed termination should be the Bi-Ba mixed plane. Therefore, all possible $\sqrt{2} \times \sqrt{2}$ reconstructions of (001) surface can be constructed by introducing Bi vacancies or adatoms on the chemically mixed surface (Fig. S8). This surface formation energy was calculated as a function of the chemical potential

of Bi (μ_{Bi}) by considering varying growth conditions. The two surface phases with 1/4-monolayer (ML) Bi vacancies or adatoms are most relevant to our experiments, since they give one Bi (i.e., bright spot) per surface supercell at the top layer as observed by STM. As shown in Fig. 7(c), the 1/4-ML vacancy (adatom) phase is prone to form at the Bi-poor (Bi-rich) condition. We cannot determine their relative stability without knowing the experimental chemical potential. However, our calculations reveal that a homogeneous distribution of top-layer Bi is energetically more favorable than inhomogeneous ones only for the vacancy phase (Table S4), which enables the formation of a regular surface reconstruction. Moreover, the vacancy phase [Fig. 7(d)] gives a simulated STM image [Fig. 7(e)] consistent with experiment. These results thus imply that the Bi vacancy phase very likely corresponds to the surface observed experimentally.

Furthermore, the existence of Bi vacancies on the surface might explain the formation of surface-stripe phases. Intuitively, the surface with Bi vacancies would experience a contractive strain that can deform the surface lattice. To determine the possible lattice deformation, we calculated the surface elastic constants of the Ba-Bi terminated surface along the high-symmetric a (or b) and a_0 (or b_0) directions (defined in Fig. 1) and obtained $C_{aa} = C_{bb} = 34.8$ GPa $\cdot$ nm and $C_{a_0a_0} = C_{b_0b_0} = 56.4$ GPa $\cdot$ nm. This result suggests that the surface lattice deformation is not isotropic but more easily happens along either the a or b direction, which lowers the surface rotational symmetry from C_4 to C_2, in agreement with our experiments. Therefore, the surface contractive strain induced by Bi vacancies is possibly a driving force of creating surface stripes. One might wonder whether the step edges of $SrTiO_3$ would impose additional strain and distort the surface stripes of $BaBi_3$. Our observations show that this factor is quite small as compared to the Bi vacancies, and never affect the surface stripes across the step edges.

The sister compound $SrBi_3$ shares similar atomic and electronic structures with $BaBi_3$ in the bulk, but displays significantly different features on the surface (Fig. S9), which can be understood by the different binding affinity of Bi on the $SrBi_3$ and $BaBi_3$ surfaces. The calculated adsorption energy of a Bi adatom on the Sr-Bi terminated surface is $\sim$0.18 eV higher than on the Ba-Bi surface. The stronger binding of Bi on $SrBi_3$ leads to two important consequences: (i) The surface phase with 1/4-ML Bi adatoms is more stable than the one with 1/4-ML Bi vacancies over a broader range of μ_{Bi} than for $BaBi_3$ [cf. Fig. 7(c) and Fig. S9(b)], making the adatom phase [Fig. S9(c)] more likely to appear in experiment; (ii) Unlike $BaBi_3$, the adatom phase favors a homogeneous distribution, while the vacancy phase does not (Table S4). The adatom phase shows STM images in agreement with our experiment [Fig. S9(d)]. Therefore, we surmise that the type of surface defects varies from Bi vacancy to Bi adatom as the coupling between Bi and substrate gets stronger from $BaBi_3$ to $SrBi_3$. The distinct STM images of point defects observed on $BaBi_3$ [Fig. 1(d)] and $SrBi_3$ [Fig. 6(a)] surfaces seem to support this scenario. Furthermore, the adatom phase would experience no surface contractive strain, which might be the reason for the absence of surface stripe on $SrBi_3$.

IV. CONCLUSIONS

Our thorough tunneling spectra, vortex core imaging and their thickness dependence, together with the comparison experiments with sister superconductor $SrBi_3$ compellingly demonstrate that superconductivity on symmetry-breaking $BaBi_3$ surface is in consistency with BCS predications for twofold symmetric order parameter, and that the superconducting pairing gaps in thin films with increased disorders appear more like V-shaped and are fairly accounted for by a model of fluctuating superconductivity. Our results show that the superconducting DOS of a fully opened s-wave gap could be profoundly modified by the symmetry breaking and disorders. This must be taken seriously for the interpretation and modeling of STM tunneling conductance spectra in superconductors with the coexistence of symmetry breaking and disorders, including high-T_c cuprates and iron-based compounds, because their possible sign-changing superconductivity is more fragile against disorders and symmetry-breaking states. This study thus may contribute to understand the tunneling conductance spectra in superconductors with rich physics of symmetry-breaking states and disorders.

ACKNOWLEDGMENTS

This work is financially supported by the Ministry of Science and Technology of China (Grants No. 2017YFA0304600, No. 2016YFA0301004, and No. 2016YFA0301001) and the National Natural Science Foundation of China (Grants No. 11774192, No. 11427903, No. 11504196, No. 11634007, No. 11674188, and No. 11334006). C.-L.S. and Y.X. acknowledge support from the National Thousand-Young-Talents Program and Tsinghua University Initiative Scientific Research Program.

W.-L.W., Y.-M.Z., and N.-N.L. contributed equally to this work.

[1] D. E. Moncton, J. D. Axe, and F. J. DiSalvo, Phys. Rev. B **16**, 801 (1977).

[2] A. M. Gabovich, A. I. Voitenko, J. F. Annett, and M. Ausloos, Supercond. Sci. Technol. **14**, R1 (2001).

[3] J. E. Hoffman, E. W. Hudson, K. M. Lang, V. Madhavan, H. Eisaki, S. Uchida, and J. C. Davis, Science **295**, 466 (2002).

[4] C. Pfleiderer, Rev. Mod. Phys. **81**, 1551 (2009).

[5] R. Comin, A. Frano, M. M. Yee, Y. Yoshida, H. Eisaki, E. Schierle, E. Weschke, R. Sutarto, F. He, A. Soumyanarayanan, Y. He, M. Le Tacon, I. S. Elfimov, J. E. Hoffman, G. A. Sawatzky, B. Keimer, and A. Damascelli, Science **343**, 390 (2014).

[6] S. Margadonna, Y. Takabayashi, M. T. McDonald, M. Brunelli, G. Wu, R. H. Liu, X. H. Chen, and K. Prassides, Phys. Rev. B **79**, 014503 (2009).

[7] M. A. Beno, L. Soderholm, D. W. Capone, D. G. Hinks, J. D. Jorgensen, J. D. Grace, I. K. Schuller, C. U. Segre, and K. Zhang, Appl. Phys. Lett. **51**, 57 (1987).

[8] Y. Ando, K. Segawa, S. Komiya, and A. N. Lavrov, Phys. Rev. Lett. **88**, 137005 (2002).

[9] M. J. Lawler, K. Fujita, J. Lee, A. R. Schmidt, Y. Kohsaka, C. K. Kim, H. Eisaki, S. Uchida, J. C. Davis, J. P. Sethna, and E. A. Kim, Nature (London) **466**, 347 (2010).

[10] T. M. Chuang, M. P. Allan, J. Lee, Y. Xie, N. Ni, S. L. Bud'ko, G. S. Boebinger, P. C. Canfield, and J. C. Davis, Science **327**, 181 (2010).

[11] J. H. Chu, J. G. Analytis, K. De Greve, P. L. McMahon, Z. Islam, Y. Yamamoto, and I. R. Fisher, Science **329**, 824 (2010).

[12] M. Yi, D. H. Lu, J. H. Chu, J. G. Analytis, A. P. Sorini, A. F. Kemper, B. Moritz, S. K. Mo, R. G. Moore, M. Hashimoto, W. S. Lee, Z. Hussain, T. P. Devereaux, I. R. Fisher, and Z. X. Shen, Proc. Natl. Acad. Sci. USA **108**, 6878 (2011).

[13] S. Kasahara, H. J. Shi, K. Hashimoto, S. Tonegawa, Y. Mizukami, T. Shibauchi, K. Sugimoto, T. Fukuda, T. Terashima, A. H. Nevidomskyy, and Y. Matsuda, Nature (London) **486**, 382 (2012).

[14] K. Nakayama, Y. Miyata, G. N. Phan, T. Sato, Y. Tanabe, T. Urata, K. Tanigaki, and T. Takahashi, Phys. Rev. Lett. **113**, 237001 (2014).

[15] S. A. Kivelson, I. P. Bindloss, E. Fradkin, V. Oganesyan, J. M. Tranquada, A. Kapitulnik, and C. Howald, Rev. Mod. Phys. **75**, 1201 (2003).

[16] C. V. Parker, P. Aynajian, E. H. da Silva Neto, A. Pushp, S. Ono, J. S. Wen, Z. J Xu, G. D. Gu, and A. Yazdani, Nature (London) **468**, 677 (2010).

[17] A. Soumyanarayanan, M. M. Yee, Y. He, J. van Wezel, D. J. Rahn, K. Rossnagele, E. W. Hudson, M. R. Norman, and J. E. Hoffman, Proc. Natl. Acad. Sci. USA **110**, 1623 (2013).

[18] P. Giraldo-Gallo, Y. Zhang, C. Parra, H. C. Manoharan, M. R. Beasley, T. H. Geballe, M. J. Kramer, and I. R. Fisher, Nat. Commun. **6**, 8231 (2015).

[19] E. Morosan, H. W. Zandbergen, B. S. Dennis, J. W. G. Bos, Y. Onose, T. Klimczuk, A. P. Ramirez, N. P. Ong, and R. J. Cava, Nat. Phys. **2**, 544 (2006).

[20] B. Keimer, S. A. Kivelson, M. R. Norman, S. Uchida, and J. Zaanen, Nature (London) **518**, 179 (2015).

[21] R. Comin, R. Sutarto, E. H. da Silva Neto, L. Chauviere, R. Liang, W. N. Hardy, D. A. Bonn, F. He, G. A. Sawatzky, and A. Damascelli, Science **347**, 1335 (2015).

[22] J. Wu, A. T. Bollinger, X. He, and I. Božović, Nature (London) **547**, 432 (2017).

[23] F. Ronning, T. Helm, K. R. Shirer, M. D. Bachmann, L. Balicas, M. K. Chan, B. J. Ramshaw, R. D. McDonald, F. F. Balakirev, M. Jaime, E. D. Bauer, and P. J. W. Moll, Nature (London) **548**, 313 (2017).

[24] B. X. Zheng, C. M. Chung, P. Corboz, G. Ehlers, M. P. Qin, R. M. Noack, H. Shi, S. R. White, S. W. Zhang, and G. K. Chan, Science **358**, 1155 (2017).

[25] E. W. Huang, C. B. Mendl, S. X. Liu, S. Johnston, H. C. Jiang, B. Moritz, and T. P. Devereaux, Science **358**, 1161 (2017).

[26] J. Chang, E. Blackburn, A. T. Holmes, N. B. Christensen, J. Larsen, J. Mesot, R. X. Liang, D. A. Bonn, W. N. Hardy, A. Watenphul, M. V. Zimmermann, E. M. Forgan, and S. M. Hayden, Nat. Phys. **8**, 871 (2012).

[27] I. Guillamón, H. Suderow, S. Vieira, L. Cario, P. Diener, and P. Rodière, Phys. Rev. Lett. **101**, 166407 (2008).

[28] C. L. Song, Y. L. Wang, P. Cheng, Y. P. Jiang, W. Li, T. Zhang, Z. Li, K. He, L. L. Wang, J. F. Jia, H. H. Hung, C. J. Wu, X. C. Ma, X. Chen, and Q. K. Xue, Science **332**, 1410 (2011).

[29] R. M. Fernandes and A. J. Millis, Phys. Rev. Lett. **111**, 127001 (2013).

[30] J. A. Slezak, J. Lee, M. Wang, K. McElroy, K. Fujita, B. M. Andersen, P. J. Hirschfeld, H. Eisaki, S. Uchida, and J. C. Davis, Proc. Natl. Acad. Sci. USA **105**, 3203 (2013).

[31] I. Zeljkovic, Z. J. Xu, J. S. Wen, G. D. Gu, R. S. Markiewicz, and J. E. Hoffman, Science **337**, 320 (2012).

[32] C. Brun, T. Cren, V. Cherkez, F. Debontridder, S. Pons, D. Fokin, M. C. Tringides, S. Bozhko, L. B. Loffe, B. L. Altshuler, and D. Roditchev, Nat. Phys. **10**, 444 (2014).

[33] S. Takei, B. M. Fregoso, H. Y. Hui, A. M. Lobos, and S. Das Sarma, Phys. Rev. Lett. **110**, 186803 (2013).

[34] K. Luna, P. Giraldo-Gallo, T. Geballe, I. Fisher, and M. Beasley, Phys. Rev. Lett. **113**, 177004 (2014).

[35] Y. Zhong, Y. Wang, S. Han, Y. F. Lv, W. L. Wang, D. Zhang, H. Ding, Y. M. Zhang, L. L. Wang, K. He, R. D. Zhong, J. A. Schneeloch, G. D. Gu, C. L. Song, X. C. Ma, and Q. K. Xue, Sci. Bull. **61**, 1239 (2016).

[36] N. Haldolaarachchige, S. K. Kushwaha, Q. Gibson, and R. J. Cava, Supercond. Sci. Technol. **27**, 105001 (2014).

[37] D. F. Shao, X. Luo, W. J. Lu, L. Hu, X. D. Zhu, W. H. Song, X. B. Zhu, and Y. P. Sun, Sci. Rep. **6**, 21484 (2016).

[38] R. Jha, M. A. Avila, and R. A. Ribeiro, Supercond. Sci. Technol. **30**, 025015 (2017).

[39] G. Kresse and J. Furthmüller, Phys. Rev. B **54**, 11169 (1996).

[40] J. P. Perdew, K. Burke, and M. Ernzerhof, Phys. Rev. Lett. **77**, 3865 (1996).

[41] G. Kresse and D. Joubert, Phys. Rev. B **59**, 1758 (1999).

[42] J. Tersoff and D. R. Hamann, Phys. Rev. B **31**, 805 (1985).

[43] Y. F. Lv, W. L. Wang, Y. M. Zhang, H. Ding, W. Li, L. L. Wang, K. He, C. L. Song, X. C. Ma, and Q. K. Xue, Sci. Bull. **62**, 852 (2017).

[44] See Supplemental Material at http://link.aps.org/supplemental/10.1103/PhysRevB.98.064511 for details on moiré superstructure, surface stripes, theoretical fits, and magnetic vortices.

[45] R. C. Dynes, V. Narayanamurti, and J. P. Garno, Phys. Rev. Lett. **41**, 1509 (1978).

[46] I. Maggio-Aprile, Ch. Renner, A. Erb, E. Walker, and Ø. Fischer, Phys. Rev. Lett. **75**, 2754 (1995).

[47] Q. Fan, W. H. Zhang, X. Liu, Y. J. Yan, M. Q. Ren, M. Xia, H. Y. Chen, D. F. Xu, Z. R. Ye, W. H. Jiao, G. H. Cao, B. P. Xie, T. Zhang, and D. L. Feng, Phys. Rev. B **91**, 104506 (2015).

[48] Z. Y. Du, D. Fang, Z. Y. Wang, Y. F. Li, G. Du, H. Yang, X. Y. Zhu, and H. H. Wen, Sci. Rep. **5**, 9408 (2015).

[49] W. L. Wang, Y. M. Zhang, Y. F. Lv, H. Ding, L. L. Wang, W. Li, K. He, C. L. Song, X. C. Ma, and Q. K. Xue, Phys. Rev. B **97**, 134524 (2018).

[50] C. Caroli, P. G. De Gennes, and J. Matricon, Phys. Lett. **9**, 307 (1964).

[51] Ch. Renner, A. D. Kent, Ph. Niedermann, Ø. Fischer, and F. Lévy, Phys. Rev. Lett. **67**, 1650 (1991).

[52] Y. X. Ning, C. L. Song, Y. L. Wang, X. Chen, J. F. Jia, Q. K. Xue, and X. C. Ma, J. Phys.: Condens. Matter **22**, 065701 (2010).

[53] D. S. Inosov, T. Shapoval, V. Neu, U. Wolff, J. S. White, S. Haindl, J. T. Park, D. L. Sun, C. T. Lin, E. M. Forgan, M. S. Viazovska, J. H. Kim, M. Laver, K. Nenkov, O. Khvostikova, S. Kühnemann, and V. Hinkov, Phys. Rev. B **81**, 014513 (2010).

[54] C. L. Song, Y. Yin, M. Zech, T. Williams, M. M. Yee, G. F. Chen, J. L. Luo, N. L. Wang, E. W. Hudson, and J. E. Hoffman, Phys. Rev. B **87**, 214519 (2013).

[55] S. P. Chockalingam, M. Chand, A. Kamlapure, J. Jesudasan, A. Mishra, V. Tripathi, and P. Raychaudhuri, Phys. Rev. B **79**, 094509 (2009).

[56] B. Sacépé, C. Chapelier, T. I. Baturina, V. M. Vinokur, M. R. Baklanov, and M. Sanquer, Nat. Commun. **1**, 140 (2010).

[57] M. Mondal, A. Kamlapure, M. Chand, G. Saraswat, S. Kumar, J. Jesudasan, L. Benfatto, V. Tripathi, and P. Raychaudhuri, Phys. Rev. Lett. **106**, 047001 (2011).

[58] B. Sacépé, T. Dubouchet, C. Chapelier, M. Sanquer, M. Ovadia, D. Shahar, M. Feigel'man, and L. Ioffe, Nat. Phys. **7**, 239 (2011).

[59] C. Richter, H. Boschker, W. Dietsche, E. Fillis-Tsirakis, R. Jany, F. Loder, L. F. Kourkoutis, D. A. Muller, J. R. Kirtley, C. W. Schneider, and J. Mannhart, Nature (London) **502**, 528 (2013).

[60] Y. Noat, V. Cherkez, C. Brun, T. Cren, C. Carbillet, F. Debontridder, K. Ilin, M. Siegel, A. Semenov, H.-W. Hübers, and D. Roditchev, Phys. Rev. B **88**, 014503 (2013).

[61] D. Dentelski, A. Frydman, E. Shimshoni, and E. G. Dalla Torre, Phys. Rev. B **97**, 100503 (2018).

[62] I. S. Burmistrov, I. V. Gornyi, and A. D. Mirlin, Phys. Rev. B **93**, 205432 (2016).

[63] B. J. Keene, Int. Mater. Rev. **38**, 157 (2013).